Journal of Structural Geology 33 (2011) 609–623

Contents lists available at ScienceDirect

Journal of Structural Geology

journal homepage: www.elsevier.com/locate/jsg

Combined quantification of anisotropy and inhomogeneity of magmatic rock fabrics – An outcrop scale analysis recorded in high resolution

Mark Peternell [a,*], M. Fátima Bitencourt [b], Jörn H. Kruhl [a]

[a] Tectonics and Material Fabrics Section, Technische Universität München, D-80333 München, Germany
[b] Centro de Estudos em Petrologia e Geoquímica, Instituto de Geociências, Universidade Federal do Rio Grande do Sul, Porto Alegre, Brazil

ARTICLE INFO

Article history:
Received 22 May 2010
Received in revised form
26 December 2010
Accepted 21 January 2011
Available online 27 January 2011

Keywords:
Anisotropy
Inhomogeneity
Rock fabric
Fractal geometry
Map-counting
MORFA

ABSTRACT

Magmatic mineral distribution patterns in a syntectonic syenite pluton have been recorded at high resolution over several square metres on quarried faces. The anisotropy and inhomogeneity of K-feldspar and mafic mineral distribution patterns have been quantified using two methods originally based on fractal geometry. (1) Map-counting, based on box-counting, illustrates an inhomogeneity on the decimetre to metre scale and highlights diffuse structures that can be related to mafic schlieren or felsic dykes that are not visible on the rock surface. (2) We have developed a mapping of rock fabric anisotropy (MORFA) method that leads to the detection of further magmatic structures that are not visible in the field. With MORFA a magmatic lineation and its variation over large areas is determined, as well as fabrics on the decimetre to 1 m scales, which possibly represent flow or fracture structures in the crystallising magma.

1. Introduction

The presence of melt affects the rheology of the Earth's crust and, vice versa, regional deformation and crustal rheological instabilities play an important role in the ascent and emplacement of melt (Hutton, 1982; Hollister and Crawford, 1986; D'Lemos et al., 1992; Petford et al., 2000; Rosenberg and Handy, 2005; Brown, 2007). The development of magmatic rock fabrics from micro- to macro-scale depends on melt properties (e.g. temperature, chemical composition), physical conditions of crystallisation (e.g. regional stress fields) and kinematics of flow (magnitude of displacement gradient). Such fabrics are generally represented by geometrical properties of material domains on different scales (patterns) – from micro- to kilo-metre scale in the case of magmatic bodies. In particular, the arrangement and orientation of crystals, crystal-size distributions and crystal shapes are of importance. In recent years, successful attempts were made to use magmatic fabrics at various scales to analyse kinematics of melt emplacement as well as deformation-cooling histories of magmatic bodies and their wall-rocks (Paterson et al., 1989, 1998; Büttner, 1999; Vernon, 2000; Rosenberg, 2001; Albertz, 2006; Zak et al., 2007; Peternell et al., 2010).

Quantification and analysis of magmatic rock fabrics face a number of difficulties: (1) The preferred alignment and concentration of crystals forming the magmatic foliation, schlieren, cumulates or magma mingling features are often too large to be recorded in a thin section; (2) magmatic fabrics are frequently too diffuse for precise conventional measurements (e.g. orientation measurements with a compass); and (3) their geometry is often irregular and, consequently, small scale measurements cannot be extrapolated to larger scales without difficulty. In many cases magmatic rock fabrics can only be described qualitatively and, therefore, methods for quantification of such fabrics are needed.

The methods available for quantification of magmatic rock fabrics include (1) measurement of magnetic susceptibility (AMS – Rochette et al., 1992; Tarling and Hrouda, 1993; Martín-Hernández et al., 2005), (2) crystal-size distributions (CSD – Marsh, 1988; Higgins, 1996, 2000), and (3) grain or mineral-phase orientation with the inertia tensor method (Launeau and Cruden, 1998), the star length distribution method (Smit et al., 1998), the normalised optimised anisotropic wavelet coefficient (NOAWC) method (Gaillot et al., 1997), the inverse SURFOR wheel (Panozzo, 1987), and the intercept method devised by Launeau and Robin (1996). However, all these methods do not quantify the complexity of a rock fabric. Complex, i.e. statistically self-similar and thus fractal, rock patterns can be quantified by fractal geometry methods

* Corresponding author. Present address: School of Earth Sciences, The University of Melbourne, Victoria 3010, Australia. Tel.: +61 3 8344 6910; fax: +61 3 8344 7761.
E-mail addresses: mark.peternell@mytum.de (M. Peternell), fatimab@ufrgs.br (M. Fátima Bitencourt), kruhl@tum.de (J.H. Kruhl).

0191-8141/$ – see front matter © 2011 Elsevier Ltd. All rights reserved.
doi:10.1016/j.jsg.2011.01.011

(Mandelbrot, 1967), such as the ruler/divider method (Mandelbrot, 1977; Kaye, 1989; Kruhl and Nega, 1996), the area-perimeter method (Kaye, 1989; Takahashi et al., 1998), or box-counting (Mandelbrot, 1977; Feder, 1988; Kaye, 1989). These fractal geometry approaches result in single numbers that are representative for the whole analysed area: thin section, rock sample or an outcrop photograph. Anisotropy and inhomogeneity, both important characteristics of rock fabrics, are accounted by the modified Cantor-dust method (MCDM, Velde et al., 1990; Volland and Kruhl, 2004; Gerik and Kruhl, 2009) and map-counting (Peternell et al., 2003, 2010; Kruhl et al., 2004), respectively. However, quantification of fabrics over larger areas and with high resolution, an essential precondition for an extended analysis of magmatic fabrics, is beyond the capabilities of these methods and has not been done so far.

In this paper we present two automated methods for high-resolution rock fabric quantification on large scales. Both methods are tested and applied on field photographs of metre-sized outcrop surfaces of the Piquiri Syenite Massif from Southern Brazil (Fig. 1).

2. Tectonic setting and structure

The last stages of the Neoproterozoic Brasiliano/Pan-African orogenic cycle in southernmost Brazil are marked by voluminous syntectonic magmatism (650–580 Ma) in a post-collisional setting. Continued magmatism under mid-crustal conditions along the Southern Brazilian Shear Belt lead to the construction of a granitic batholith, which parallels the coast from southern Brazil to Uruguay (Fig. 1a).

The Piquiri Syenite Massif (Fig. 1b) is a crescent-shaped pluton with an area of approximately 150 km^2, dated at 611 $\pm$ 3 Ma (Pb–Pb on magmatic zircons; Philipp et al., 2002). It is intrusive into high-grade gneisses and syntectonic granitoids, medium- to low-grade metapelites, and acid metavolcanic rocks.

Medium- to coarse-grained alkali feldspar-syenites and quartz-syenites are the main lithological types, with fine-grained monzonitic and syenitic varieties identified at the pluton margins. In the pluton centre there are co-genetic syenogranites and alkali feldspar-granites (Nardi et al., 2008). A magmatic foliation is present throughout the pluton, and is better developed in the internal part rather than in the outer rim. The foliation is mostly sub-vertical (Fig. 1b) and its orientation is generally conformable to the pluton's external contacts.

The main syenite (Figs. 1b and 2) contains cm-scale K-feldspar crystals (~60%) and mafic aggregates composed of micrometre to millimetre-sized pyroxene (3–10%), amphibole (5–20%), titanite, apatite, opaques, and minor amounts of biotite. The K-feldspar crystals are aligned and together with the elongate mafic mineral aggregates define the magmatic foliation (Fig. 2e, f). No linear fabric is visible, either at outcrop or thin section scale (Fig. 2b, c). Local variations of magmatic foliation intensity and geometry at outcrop scale are indicated by planar or sigmoidal geometries of K-feldspar alignment (Fig. 3a) and narrower spacing of foliation planes within cm- to dm-wide zones. A magmatic foliation is oriented either parallel or at high angles to a compositional banding that is locally present as an early-formed structural feature. The mafic layers, composed of coarse-grained cumulus pyroxenes and amphiboles, are either continuous or disrupted, giving rise to a local schlieren layering (Fig. 3b). The segregational character of such layers is enhanced by the presence of country-rock xenoliths, chilled-margin fragments, mafic cumulatic autoliths, and microgranular enclaves, as described by Nardi et al. (2007). Approximately equal, cm-sized K-feldspar crystals are locally concentrated in elongate portions where mafic aggregates are subordinate and interstitial; these are interpreted as felsic cumulates.

No solid-state deformation structures are visible (Fig. 2c, f). Rare micro-cracking of K-feldspars, weak chessboard subgrain patterns in interstitial quartz, and local flame albitization of feldspar rims at the contact between two feldspars occur.

3. Sampling and image processing

For the analysis of rock fabric inhomogeneity and anisotropy field photographs of the syenite were taken at two sites within a large quarry (Fig. 2). The active part of the quarry (Fig. 2a) consists of vertical and subhorizontal surfaces cut parallel and perpendicular to the magmatic foliation. In contrast, the inactive part of the quarry, approximately 500 m to the southwest (Fig. 2d) contains subhorizontal surfaces, generally more irregular than in the active part, and partly weathered. The magmatic foliation is sub-vertical with slightly variable strikes, from NE–SW in the active quarry (Fig. 2a) to approximately E–W in the inactive one (Fig. 2d).

For large-scale analyses several digital colour photograph series from different rock surfaces of the syenite were taken within the quarries and stitched together. Sections 1 and 2 are photograph series from freshly sawn vertical surfaces of the active quarry (Figs. 2a and 4a, b). Section 3 represents the partly weathered base of an old berm in the inactive quarry (Figs. 2d and 4c, d). All three sections show clear evidence of schlieren and of up to approximately 10 cm sized mafic microgranular enclaves. In Section 3, an elongate body of more felsic and coarser grained syenite is crosscut by the main foliation (Fig. 4c, d). For cm-scale analysis, an approx. 0.2 m $\times$ 0.2 m $\times$ 0.3 m oriented sample was taken from the inactive quarry. The sample was sawn parallel (sample 1, Fig. 2b) and perpendicular (sample 2, Fig. 2e) to the NE–SW striking foliation and scanned. In addition, 11 polished thin sections were prepared for micro-scale analyses; 9 parallel to the magmatic foliation (Fig. 2c, but taken parallel to sample 1 to enable the investigation of a similar area) and 2 approximately parallel to Section 3 (Fig. 2f).

The photographs were stitched together and were converted to grey-scale images in order to separate the mafic and felsic phases of the syenite. The image processing is illustrated in Fig. 5 (exemplified on one input image) and contains 3 main steps: (1) An image cleanup using Photoshop® followed by the image stitching procedure with PtGui software, (2) a mineral segmentation algorithm based on a water-flow/watershed model (Vincent and Soille, 1991; Kim et al., 2002) and (3) conversion of the images into black-and-white images. White in the output image (Fig. 5) represents the felsic phases (K-feldspar and minor amounts of quartz), and black represents the mafic minerals (pyroxene, amphibole, titanite, opaques, and minor amounts of biotite). Within this work, the distribution and orientation of microgranular mafic enclaves were not investigated and therefore, they were manually erased in the grey-scale images (Fig. 6). As a consequence, the enclaves are treated as artificial impurities.

4. Quantification methods

The two applied methods are map-counting (Peternell et al., 2003, 2010; Kruhl et al., 2004) and the new mapping of rock fabric anisotropy (MORFA) method (Peternell, 2007). For the first time, automated versions of both methods are used. The software (Matlab® functions and scripts) *map-counting* and *MORFA* are available from the corresponding author.

4.1. Map-counting

Map-counting is a modified box-counting method to determine inhomogeneities in object distribution patterns. Box-counting (Mandelbrot, 1977) is a powerful tool to quantify the degree of

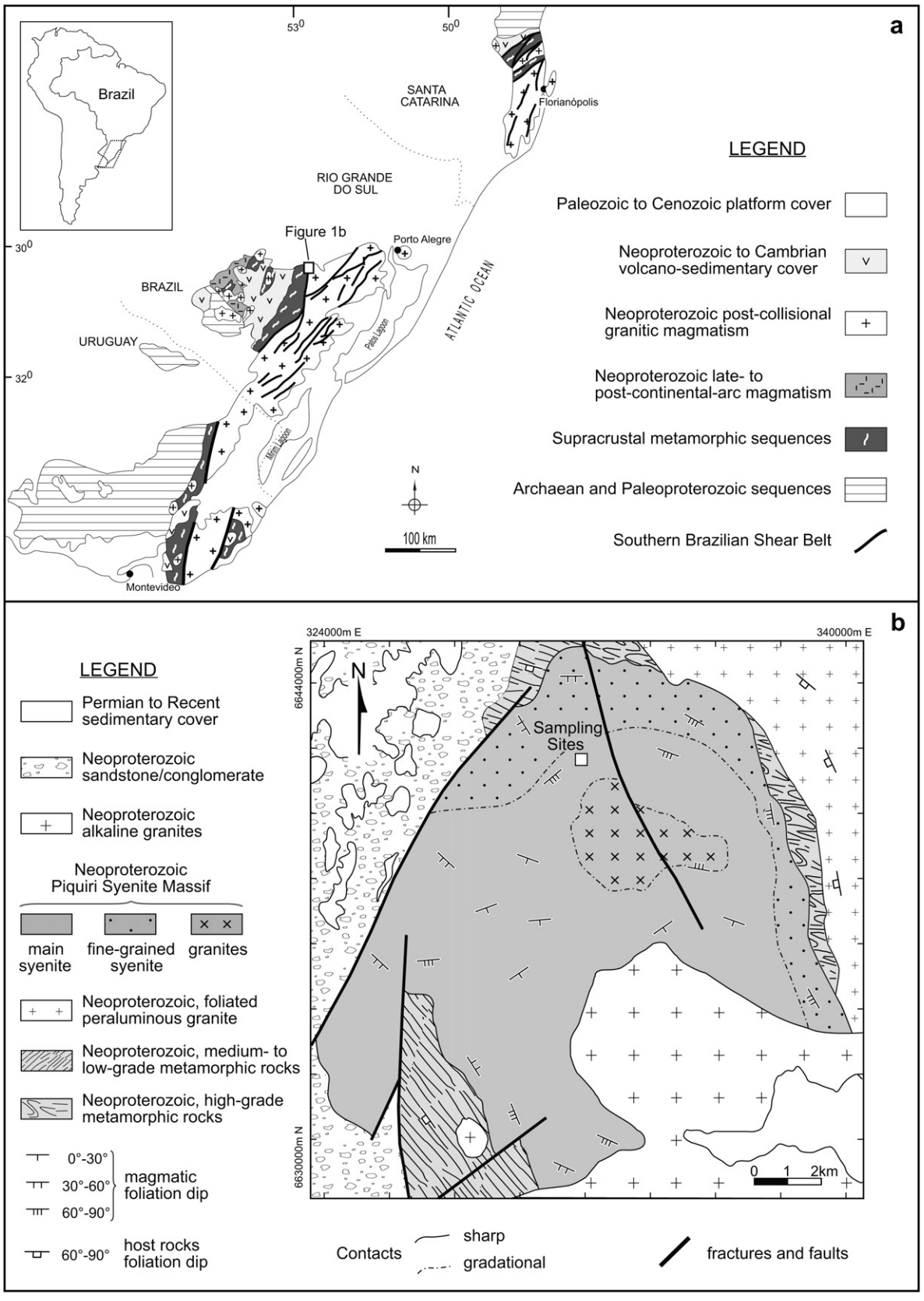

Fig. 1. (a) Geological context of southern Brazil and Uruguay; (b) Geological map of the Piquiri Syenite Massif; modified after Porcher (2000) and Nardi et al. (2008).

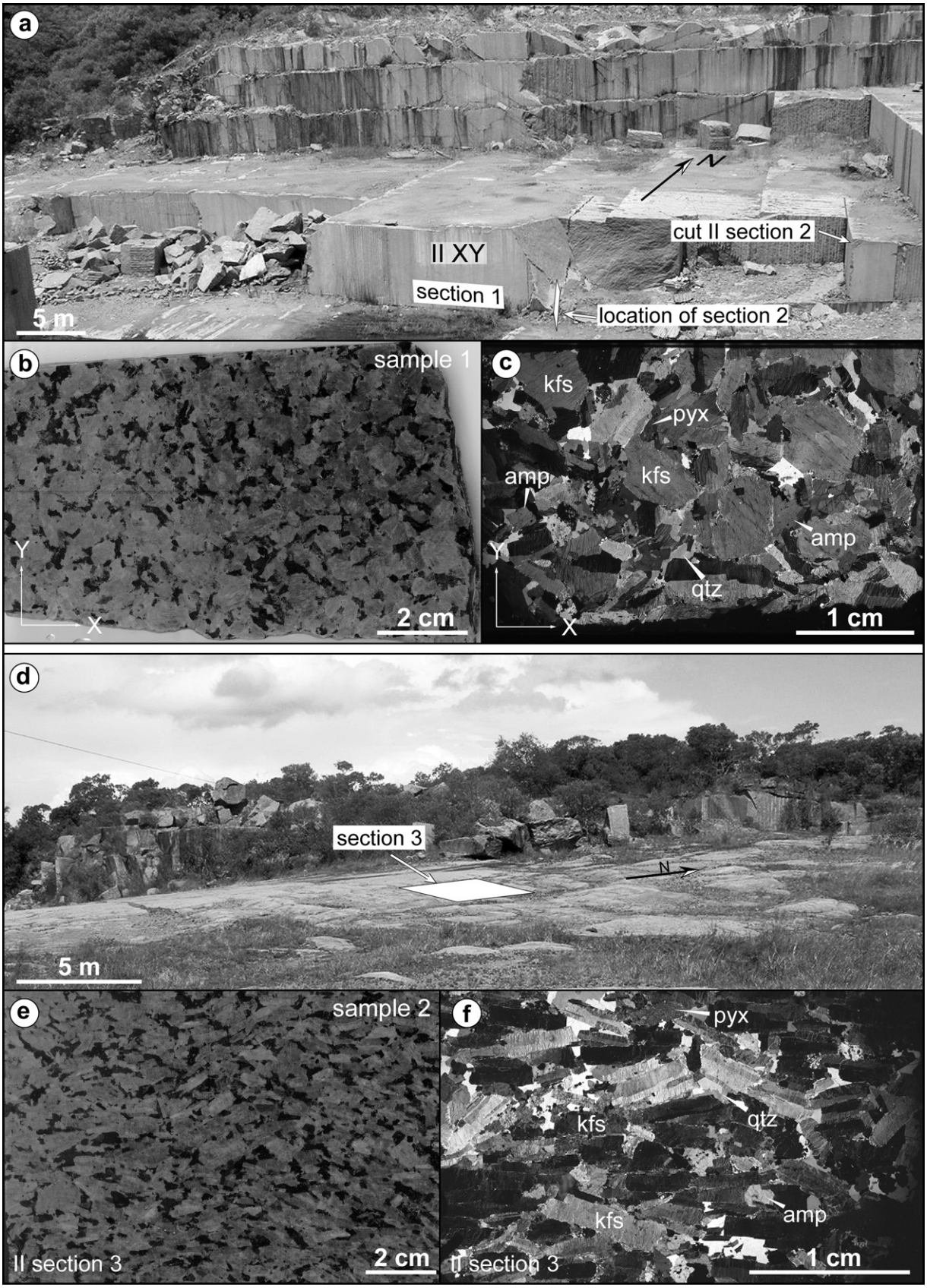

Fig. 2. Investigated quarry in the Piquiri Syenite. (a) Active part of the quarry with position and approximate sizes of photographed sections: section 1 – parallel to XY (the magmatic foliation) and section 2 – perpendicular to section 1. The block containing section 2 is already exhausted; (b) scanned Piquiri Syenite rock slab and (c) photomicrographs from a cut parallel to the magmatic foliation with no visible magmatic lineation (sample KR4759B); (d) inactive part of the quarry located approximately 500 m southwest from (a); the position of photographed section 3 – perpendicular to sections 1 and 2, is indicated; (e) scanned Piquiri Syenite rock slab and (f) photomicrographs from a cut II section 3; the feldspar crystals are well aligned with planar and slightly sigmoidal geometries and define the magmatic foliation (sample KR4759B).

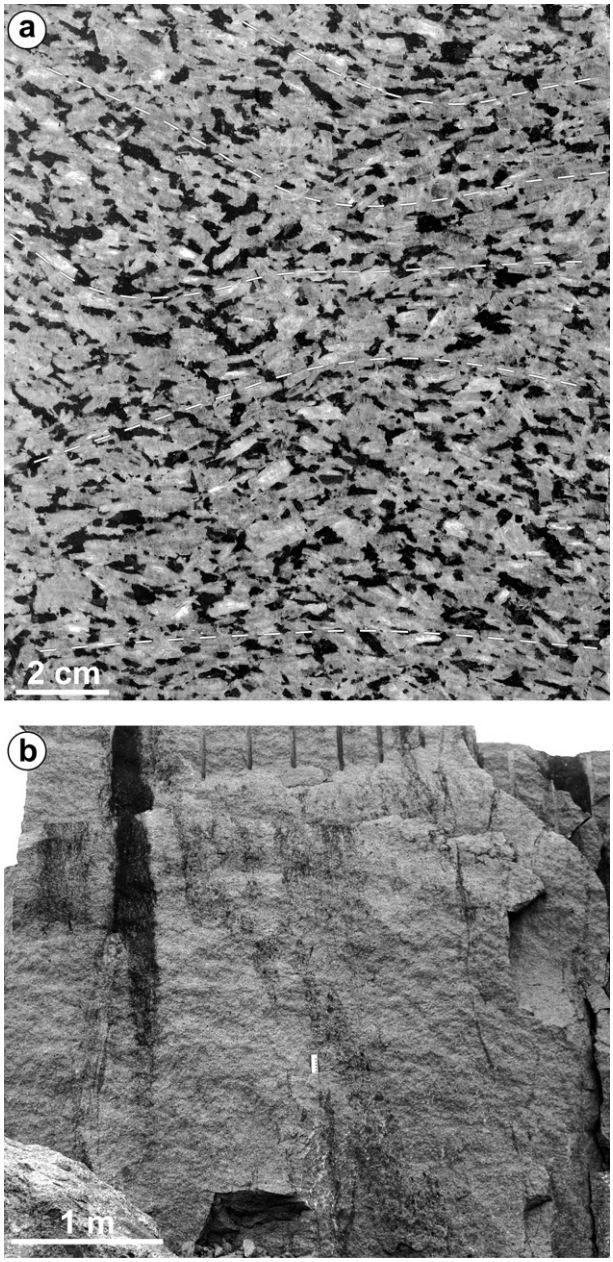

Fig. 3. Structures in the Piquiri Syenite; (a) scanned rock slab from a cut perpendicular to the magmatic foliation. The white lines indicate the planar or sigmoidal geometries of K-feldspar alignment; (b) outcrop photograph from a vertical rock surface of the syenite showing schlieren layering. The schlieren are either continuous or disrupted and locally very diffuse and/or complex.

complexity of a pattern, i.e. the "ability of a pattern to fill the space" (Mandelbrot, 1982). Application of the method results in a positive real number D_b, the box-counting dimension, defined by the relation

$$N(r) \cong r \cdot \exp D_b. \quad (1)$$

Therefore, the value of D_b quantifies the pattern's complexity. D_b of 2D patterns ranges between 0 and 2, the Euclidian dimensions of a point and a plane, respectively. Details of the method are described in numerous textbooks (Feder, 1988; Kaye, 1989; Turcotte, 1989). The pattern complexity in the studied syenite mafic mineral aggregates is caused by the spatial distribution of aggregates and their shapes.

Since box-counting results in a single number that determines the complexity for the whole analysed pattern, variation in complexity within the pattern, i.e. inhomogeneity, cannot be determined. In order to overcome this limitation, a gliding-window procedure can be added to box-counting. The combination of both methods is named map-counting (Peternell et al., 2003, 2010; Kruhl et al., 2004) and later studies using a similar gliding box-counting procedure (Hodkiewicz et al., 2005; Ford and Blenkinsop, 2008). The principles of map-counting is illustrated in Fig. 7a. During the map-counting procedure a square (window) of specific size r is shifted over the structure in pre-defined steps s. r is chosen depending on the size of the investigated mafic aggregates and on the relative distance between them. In order to comprise a large number of mafic aggregates for statistical accuracy of the resultant box-counting dimensions, r is set to 0.1 m, and therefore ~10 times larger than the largest aggregate sizes of the analysed areas. The gliding distance $s = 5$ mm is chosen to produce results with a very high resolution.

D_b is determined for each position of the gliding window and presented as colour-indexed pixels of size s. The colour is given by a colour lookup table (Fig. 7a). Different colours reflect the inhomogeneity of space-filling of the mafic mineral-aggregate pattern. Peternell and Kruhl (2009) suggest to consider a D_b value as valid for high accuracy if its correlation coefficient $R^2 \geq 0.998$ and they rejected a measurements if $R^2 \leq 0.994$. Nevertheless, within their study values between 0.995 and 0.997 didn't occur. Our R^2 data sets consist of very few $R^2 < 0.997$ and almost none <0.994 (see Supplementary material). Therefore, we lean on their suggestion but, decided that $R^2 \geq 0.997$ seemed to be sufficient. This is based on the observation that neighbouring measurements with R^2 values between 0.997 and 0.998 and $R^2 > 0.998$, respectively, lead to the same *box-counting* dimensions. Within this study a measurement-failure criteria of $R^2 < 0.994$ suggested by Peternell and Kruhl (2009) can neither be confirmed nor rejected as almost all measurements are above this threshold.

In all former studies map-counting was applied manually and the D_b distribution was presented qualitatively in contour maps produced by a kriging procedure (Peternell et al., 2010). The *map-counting* software is now applicable and, therefore, distribution patterns of mafic mineral aggregates are determined over areas of several square metres. Structures such as schlieren, magmatic folds, faults, dykes and overprinting structures caused by magmatic flow can be determined although they cannot be readily perceived by the human eye. In addition, the colour-indexed pixel maps for the D_b distribution (Fig. 7a) result in a quantitative presentation of the results.

4.2. Mapping of rock fabric anisotropy

The mapping of rock fabric anisotropy (MORFA) method is a combination of the modified Cantor-dust method (MCDM, Velde et al., 1990; Volland and Kruhl, 2004) and a gliding-window procedure. The automated method is applicable to 2 colour images of all sizes, e.g. mafic mineral aggregate- and K-feldspar images. The principles of the MCDM for single image analyses are described by Volland and Kruhl (2004) and Gerik and Kruhl (2009).

During the MORFA procedure a circle of specific diameter d is shifted over the structure in pre-defined steps s (Fig. 7b). The circle diameter depends on the size of the investigated objects and on the distances between them. In this study, a circle radius of 0.10 m is chosen and therefore, ~10 times larger than single feldspar crystals (Fig. 2b, e). This increases the statistical significance of the MORFA results as a large number of grains is analysed for each circle-window. The choice of the gliding distance s depends on the target resolution and the processing time of the method. In the studied

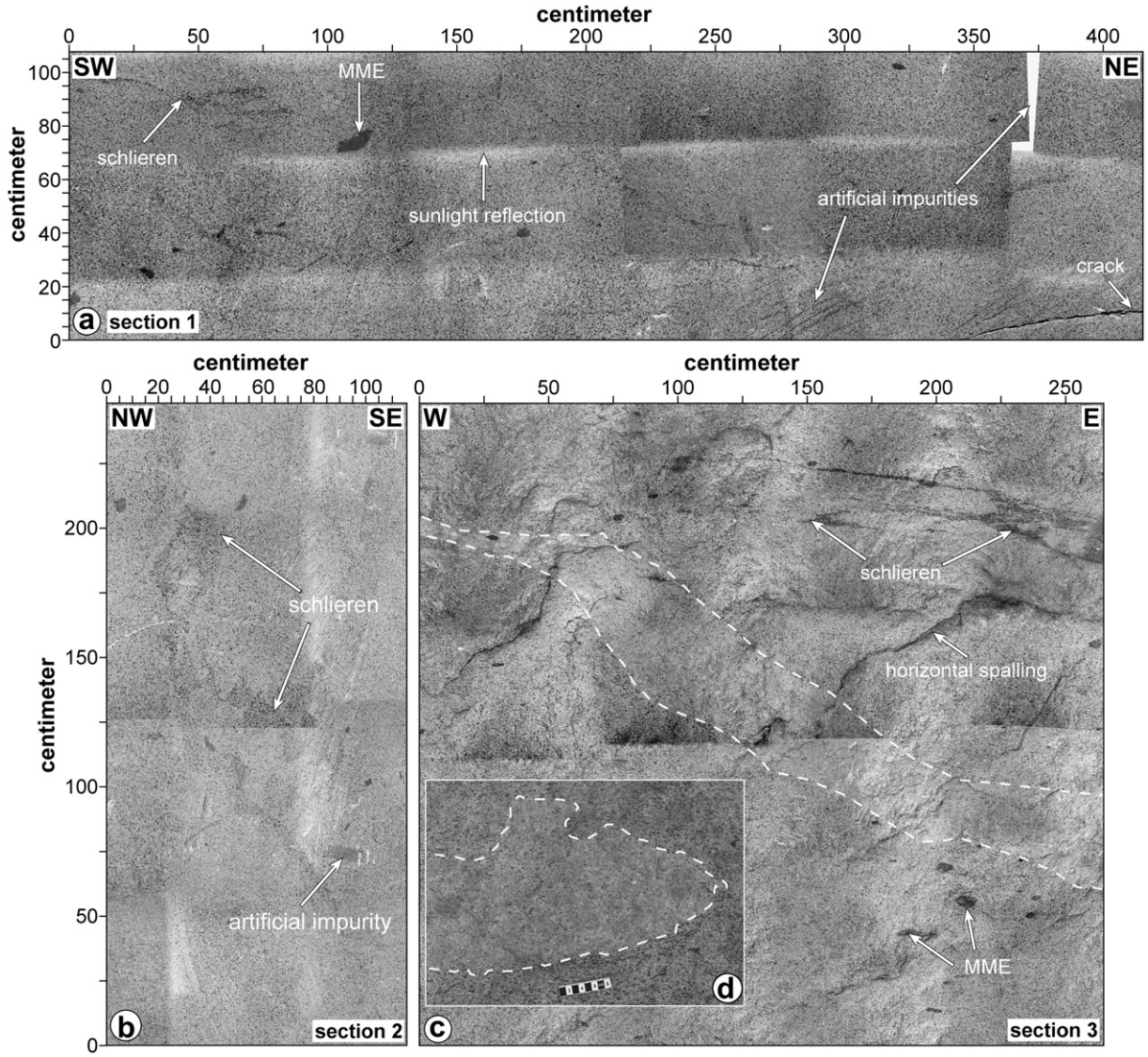

Fig. 4. SW–NE (a), NW–SE (b) and W–E (c) oriented image of the investigated outcrop surface sections 1–3 (Fig. 2). The images are based on 18 (a), 12 (b) and 24 (c) single-surface orthogonal photographs, respectively. (a) 4.2 × 1.1 m large vertical rock surface, sawn parallel the magmatic foliation of the syenite. Impurities like sunlight reflections, artificial scratches by the saw, a hole or a rock crack are indicated. Diffuse schlieren are visible as well as mafic microgranular enclaves (MME) of different sizes. The magmatic foliation-related lineation is not visible on this section. (b) 1.1 × 2.5 m sized section 2, schlieren and artificial impurity are indicated. (c) 2.7 × 2.5 m sized subhorizontal section 3. This surface is not sawn and therefore more irregular, resulting in surface-parallel rock spalling which causes shadows on the rock surface. An elongate felsic body running from upper left to lower right in section 3 (dashed line) consists of a relatively higher amount of K-feldspar crystals, as shown in more detail in inset. (d) The photo shown in the insert is taken from right end of the felsic body not shown in (c).

Syenite *s* is chosen as 5 cm in order to result in a high resolution of anisotropy distribution maps and to reduce processing times to no more than ~1 day for each analysis.

The MCDM implemented in *AMOCADO* (Gerik and Kruhl, 2009) is applied to each circle. The method can be applied on both fractal and non-fractal patterns by a slight change in procedure described by Gerik and Kruhl (2009). For this study we use the non-fractal procedure only. During this procedure the length of segments, cut by scanlines out of the pattern within a circle, are plotted vs. their number in a semi-logarithmic plot (Fig. 8a). The absolute value of the slope *m* of the regression line is plotted as a distance from a centre towards the outside, resulting in a point symmetric and more or less elliptical point distribution (Fig. 8b). For each of these point distributions, the MCDM determines a best-fit ellipse and three values: the correlation coefficient R^2, the anisotropy intensity value and the orientation of the best-fit ellipse. R^2 describes the significance of the determined fit ellipse. In this study, all measurements result in $R^2 > 0.9$ ($R^2 \in [0; 1]$) except for those related to the position of the mafic microgranular enclaves, the image gap, and the crack shown in Fig. 4 with $R^2 < 0.9$. The lower R^2 values are caused by the artificial white areas in the grey-scale templates for the MORFA analysis (Fig. 6).

The anisotropy intensity is defined as the ratio *a*/*b* of the ellipse's principal axes, and the angle γ as the orientation of the ellipse's short axis clockwise from the Y (Fig. 2a–c) direction. This short axis defines the general direction with the smallest slope *m* of the regression line in Fig. 8a and named as the direction of short ellipse-axis of anisotropy of pattern complexity (short axis of anisotropy – SAA). It is represented for each measurement as a black bar (Fig. 7b). The anisotropy intensity values in the centre of each square are presented as colour-indexed pixels of size *s* and the colour given by a lookup table (Fig. 7b). Different colours reflect regions of different pattern anisotropy intensity.

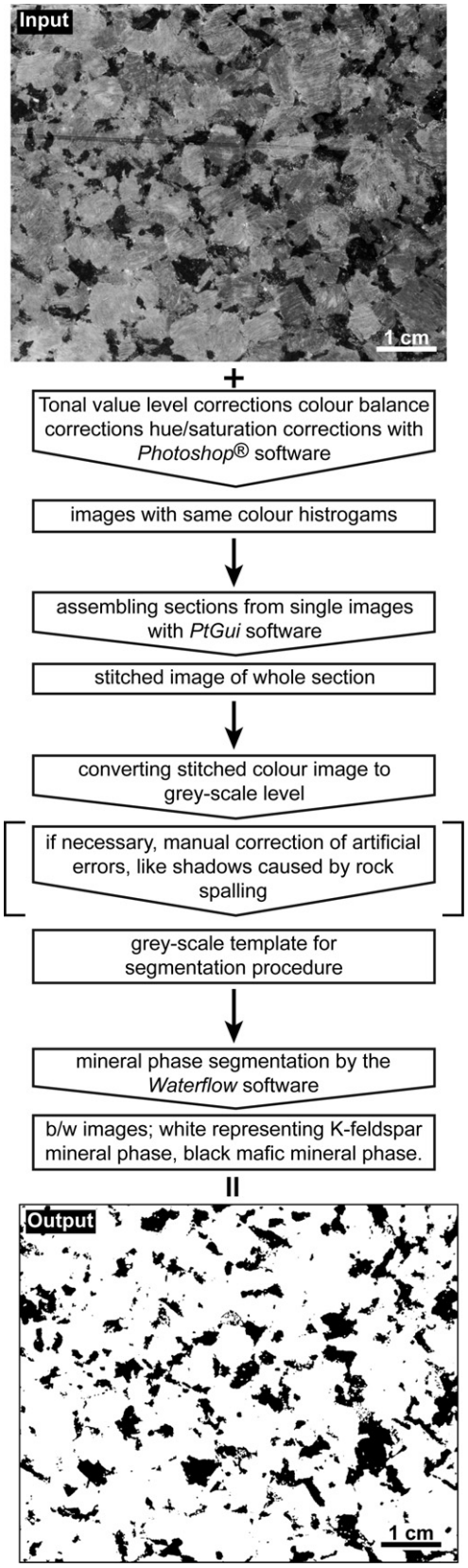

Fig. 5. Workflow of image cleaning and preparation for mineral-phase segmentation procedure.

4.3. Accuracy of map-counting and MORFA

The box-counting method (Mandelbrot, 1977), on which map-counting is based, is well understood and was used in many previous studies (e.g. Hirata, 1989; Walsh and Watterson, 1993; Velde, 1999; Bonnet et al., 2001; Kruhl et al., 2004; Peternell and Kruhl, 2009). In particular Peternell and Kruhl (2009) discuss the significance of box-counting results for magmatic mineral distribution patterns in relation to image quality and a statistical parameter evaluating the box-counting dimension. Following their measuring procedures the box-counting dimensions determined in this study are very accurate and suitable for map-counting.

The accuracy of the MCDM, the base for map-counting on natural patterns, was tested before by Gerik and Kruhl (2009). These authors compare MCDM results from a single measurement with *Intercepts* (Launeau and Robin, 1996), a computer program to determine pattern anisotropy based on image analysis. Nevertheless, to evaluate the precision of MCDM and its strength in analysing large scale, diffuse and complex rock fabrics as well as large data sets, the results from mineral distribution patterns of the Piquiri Syenite Massif from different rock cuts are compared with (1) manually measured K-feldspar long-axis distributions, (2) K-feldspar α indicatrix-axis distributions and (3) the results of *Intercepts*. In this study, MCDM was favoured over *Intercepts* because of its ability to determine pattern anisotropy in two phase images (K-feldspar and mafic aggregates) for both minerals independently, which is not possible with *Intercepts* (Gerik and Kruhl, 2009). In addition, batch processing of thousands of images is easy with the Matlab-coded MCDM.

The azimuthal directions of K-feldspar long-axes are measured on 9 thin sections parallel to the surface of sample 1 (Fig. 2b, c) and the results are presented in a rose diagram (Fig. 9a). The distribution shows a weak but distinct maximum with a mean vector direction $\theta = 100^{\circ}$. This maximum of K-feldspar long-axis orientations is interpreted as a magmatic lineation. To test the statistical significance of the data, circular statistic analyses after Piazolo and Passchier (2002) have been applied. The K-feldspar long-axes distribution passed the Rayleigh test and is therefore taken as a non-random distribution. The very low kappa value of 0.35 indicates a very weak and almost invisible ($\kappa < 1$) but geologically significant ($\kappa > 0.2$) preferred orientation of the long-axes. The high 95% confidence level (CL) of 33° confirms the very weak preferred orientation.

Universal-stage measurements on two thin sections perpendicular to Section 1 (II to tectonic XY) lead to α indicatrix-axis preferred orientations (Fig. 9b). The results are rotated to the XY plane in order to be comparable with the feldspar long-axis orientation. The K-feldspar α indicatrix-axes are distributed along a broad girdle with a distinct maximum (Fig. 9b). Since α deviates only by 3–12° from [100] for orthoclase (Tröger, 1952) the α maximum also represents the [100] maximum. Both maxima, that of the morphological long-axes (Fig. 9a) and that of the α indicatrix-axes preferred orientation (Fig. 9b), coincide remarkably well with the SAA from the MCDM applied on the surface from sample 1 (Figs. 2b and 9c) and represent a weak but clear K-feldspar shape preferred orientation (SPO), i.e. in case of the section 1-parallel surface (II XY) the magmatic lineation. Because of the subhorizontal magmatic lineation, sections 1–3 (Figs. 2a, d and 4) are regarded parallel to strain XY, YZ and XZ.

In order to evaluate the accuracy of the MCDM statistically, 120 K-feldspar mineral distribution patterns (each ~20 cm^2 large) from the Piquiri Syenite Massif were analysed with both, the MCDM and *Intercepts*. The differences in the SPO, named misorientation, between both methods are illustrated in frequency distribution histograms (Fig. 9d); differences in anisotropy intensities are

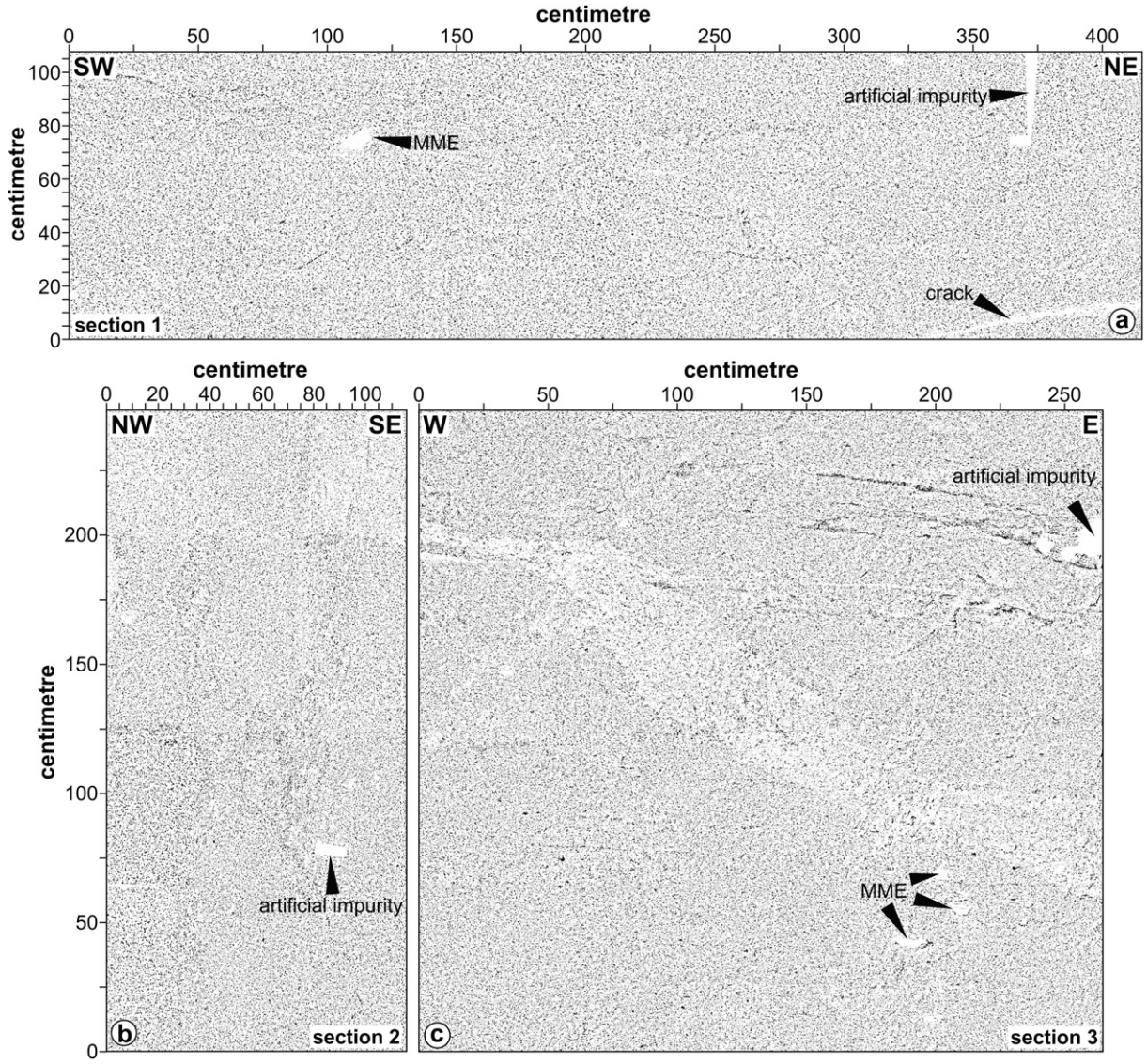

Fig. 6. Black (mafic phase) and white (mainly feldspar) images of sections 1–3 as a result of image processing shown in Fig. 5. Artificial impurities and cracks are indicated. Mafic microgranular enclaves (MME) are treated as impurities and therefore were manually coloured in white.

presented in Fig. 9e. The misorientations are small (10.3° mean) for mineral distribution patterns from the surface parallel to the magmatic foliation (Fig. 4a) and very small for surfaces parallel to strain YZ (Fig. 4b; 5.6° mean) and XZ (Fig. 4c; 5.5° mean). The weakly developed magmatic lineation explains the higher misorientations for the foliation-parallel cut. Whether one of the two methods leads to more accurate results cannot be tested within this study because both are based on image analysis techniques and, therefore, sensitive to simplifications of the natural patterns during the digitising process, i.e. wrong phase labelling or rock surface impurities (Fig. 4). Taking this into account, the results from Fig. 9d indicate a mean accuracy of $<5^\circ \pm 5$ for the MCDM in case of syenite. The anisotropy intensities for all measurements are almost identical for both methods (Fig. 9e).

5. Results

5.1. Map-counting

Map-counting applied on mafic mineral-aggregate distribution patterns from the Piquiri Syenite Massif (Fig. 2a, d) results in a colour-coded map of box-counting dimensions D_b (Fig. 10). The D_b values for the three rock surfaces (sections 1–3) range between 1.15 (white colours) and 1.45 (blue–purple colours). This range represents the pattern inhomogeneity, i.e. the variation of pattern complexity over the analysed area. The variation is not random but forms a diffuse pattern dominated by relatively low box-counting dimensions on section 1, i.e. parallel to the magmatic foliation, and relatively higher ones on the sections 2 and 3 (Fig. 10). Small values between 1.15 (white–yellow) and ~1.22 (yellow–green) correspond to the more felsic dyke-shaped domain observed on the subhorizontal surface (section 3; Figs. 4c and 10c). However, the low D_b values do not shape the elongate figure completely. It is interrupted by regions of higher D_b between ~1.22–1.32 (green) and ~1.32–1.40 (red). In addition, the lower right part of the more felsic dyke-shaped domain (section 3) is displaced twice by ~15–20 cm, respectively, indicating sinistral sense of movement in E–W direction (Fig. 10c, black dashed lines and arrows). These interruptions as well as the very small D_b values on the upper corners of section 2 (Fig. 10b) are not supported by field observations. In addition to the regions with low D_b values, the strain YZ- and XZ-parallel sections are covered by more or less irregular spots

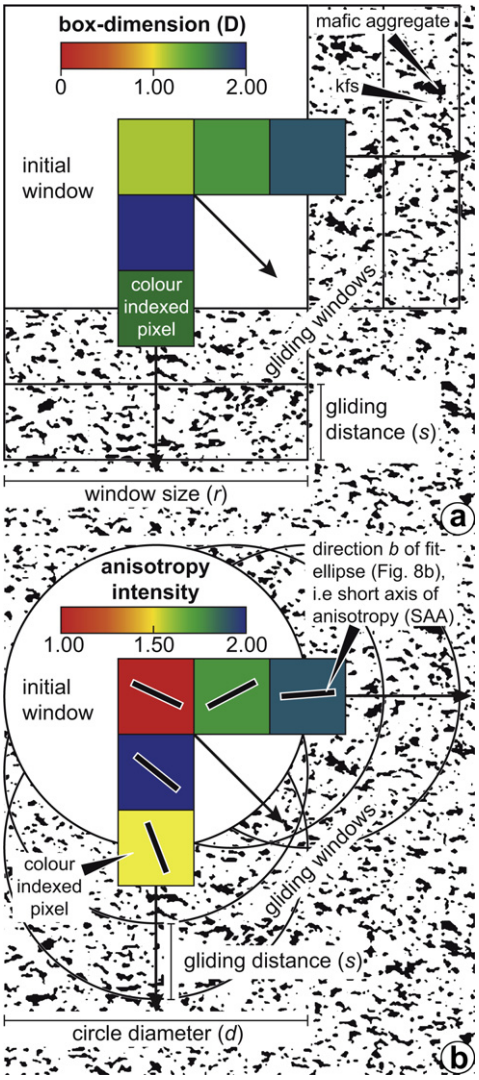

Fig. 7. Principles of the high-resolution map-counting and mapping of rock fabric anisotropy (MORFA) methods applied to mafic aggregate pattern of the Piquiri Syenite. (a) Map-counting method modified after Peternell et al. (2003, 2010) and Kruhl et al. (2004). An initial window (white square) of specific size r is shifted in two orthogonal directions over the structure, with steps of length s (gliding-window procedure). The mineral distribution pattern within each single square is analysed by box-counting. The box-counting dimension D_b is plotted in the centre of each related window as a colour-indexed pixel with a size equal the gliding distance s. In case of high-resolution map-counting $s = 0.05$ times r. Notice, in 2D analysis $D_b \in [0; 2]$. D_b determines the spatial arrangement of the analysed components (mineral aggregates), i.e. their space-filling ability. The resulting colour map of box-counting dimensions determines the variation in the space-filling ability of the different patterns, i.e. the pattern inhomogeneity of the whole analysed area. (b) MORFA method after Peternell (2007). A window (white circle) of a specific diameter d is shifted with a specific gliding distance s in two orthogonal directions over the structure. The pattern each circle is analysed by the modified Cantor-dust method. The result for each circle is plotted in the circle centre as a colour-indexed pixel with a pixel size equal the gliding distance s and a black bar. In case of high-resolution MORFA $s = 0.25$ times r. Each colour represents the anisotropy intensity (ratio a/b of a fit ellipse, Fig. 8b) of the analysed mineral-phase pattern. The black bar represents the direction of the short axis b from a fit ellipse (Fig. 8b), i.e. the direction of anisotropy of pattern complexity (short axis of anisotropy – SAA) for each measurement. In case of the Piquiri Syenite the SAA is equal to the crystal shape preferred orientation; Coloured figure available in the online version.

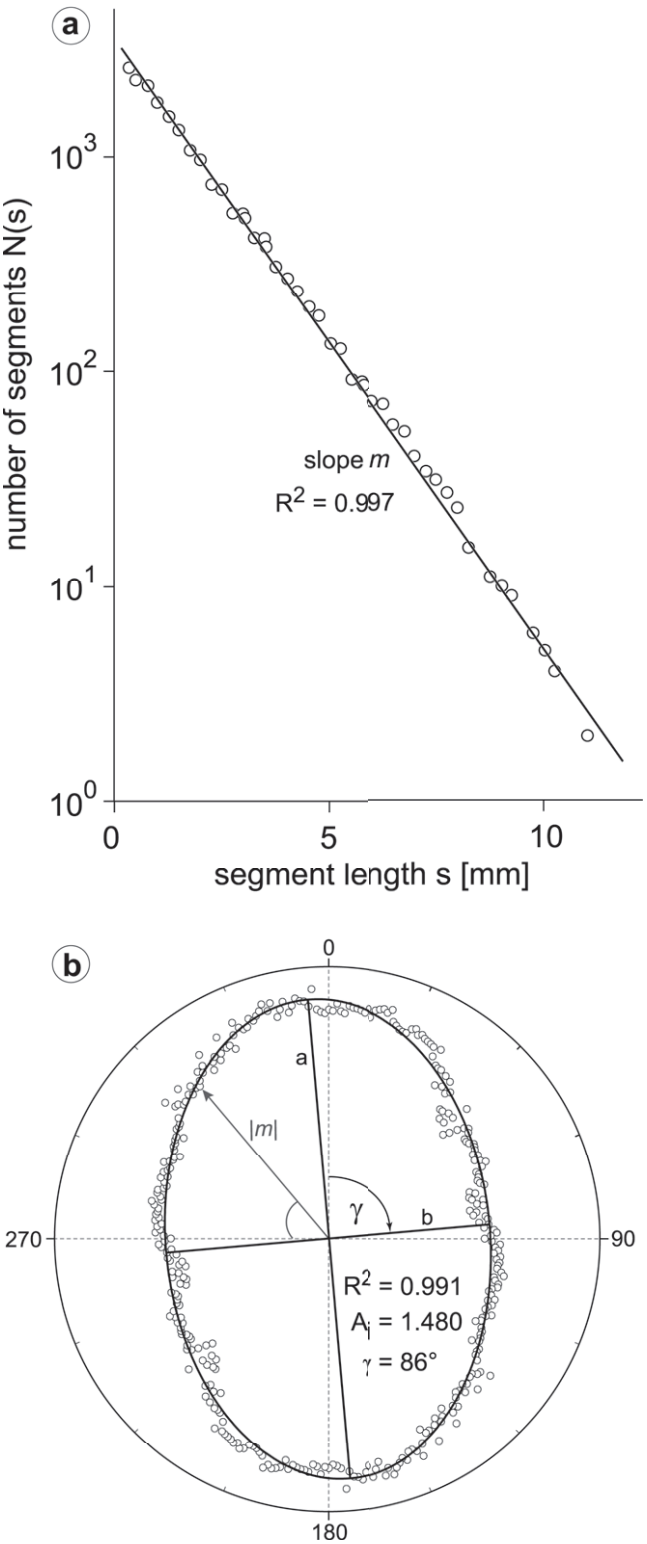

Fig. 8. Principles of the modified Cantor-dust method (MCDM, Volland and Kruhl, 2004). (a) The lengths of segments, cut by scan-lines out of the pattern within a circle, are plotted vs. their number in a semi-logarithmic plot. The value of the regression line m quantifies the segment-length distribution for one orientation of the scan-lines. (b) Graphical representation of all m in relation to their scan-line directions. Data points are fitted by an ellipse with semi axis a and b. Axial ratio a/b, i.e. the ellipticity, measures the intensity of pattern anisotropy. The orientation of b (SAA) is given by the angle γ. In case of the Syenite b represents the SPO of the investigated pattern.

of relatively high D_b values (red–blue). These areas partly match the shapes of schlieren structures determined in the field (Figs. 4b, c and 10b, c). On the upper right corner of section 3 two planar structures are outlined by dashed lines (Fig. 10c). These planar structures correspond to schlieren structures (Fig. 4c) which are

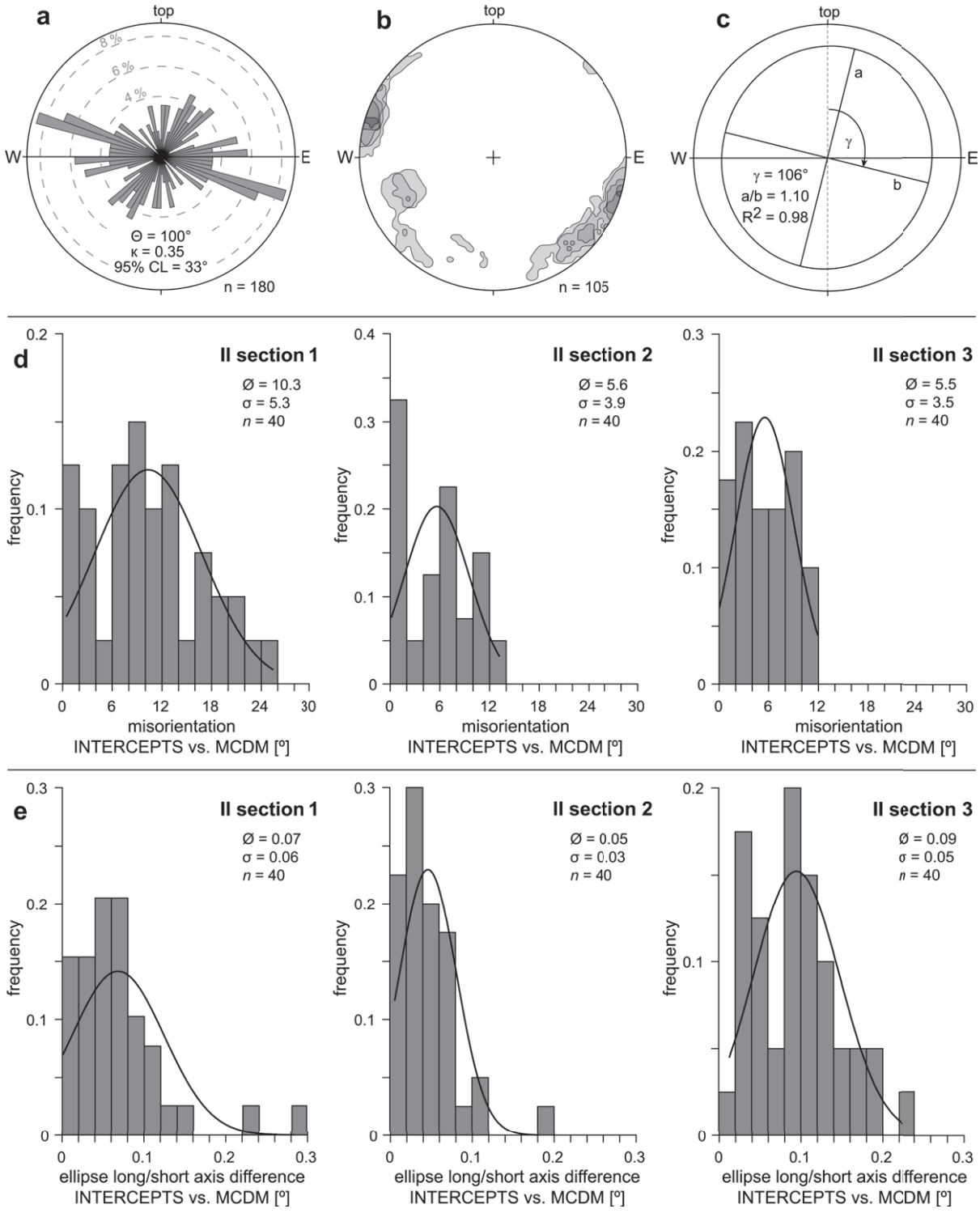

Fig. 9. Shape preferred orientation measurements of K-feldspar from the Piquiri Syenite and a comparison between *Intercepts* and the MCDM. n = number of measurements. (a) Rose diagram of azimuthal directions of K-feldspar long-axes measured on nine XY-parallel thin sections from sample KR4759B (Fig. 2c). The foliation strike is indicated (E–W) The Raleigh test confirms a non-random distribution with very low kappa value κ, a mean vector value θ and, 95% confidence level (CL). (b) Preferred orientation of K-feldspar α indicatrix-axes; universal-stage measurements from two YZ-parallel thin sections of sample KR4759B. Data are rotated to the XY plane. Equal area projection, lower hemisphere; contours = 2 [multiples uniform distribution]. (c) MCDM applied on the K-feldspar distribution pattern on the XY plane of sample KR4759B (Fig. 2c). Best ellipse fit for the MCDM result is described by its correlation coefficient R^2. Ratio a/b = anisotropy intensity, b = SAA parallel to SPO, with relative orientation to the reference system given by the angle γ. (d) Frequency histograms of differences in SPO determined by *Intercepts* vs. MCDM, related to sections 1–3. (e) Frequency histograms of differences in anisotropy intensity a/b determined by *Intercepts* vs. MCDM, related to sections 1–3. For (d) and (e) methods are applied on 120 randomly chosen 20 × 20 cm sized K-feldspar patterns from sections 1–3 (Figs. 3 and 4). The standard deviation σ for each diagram is indicated by a black line.

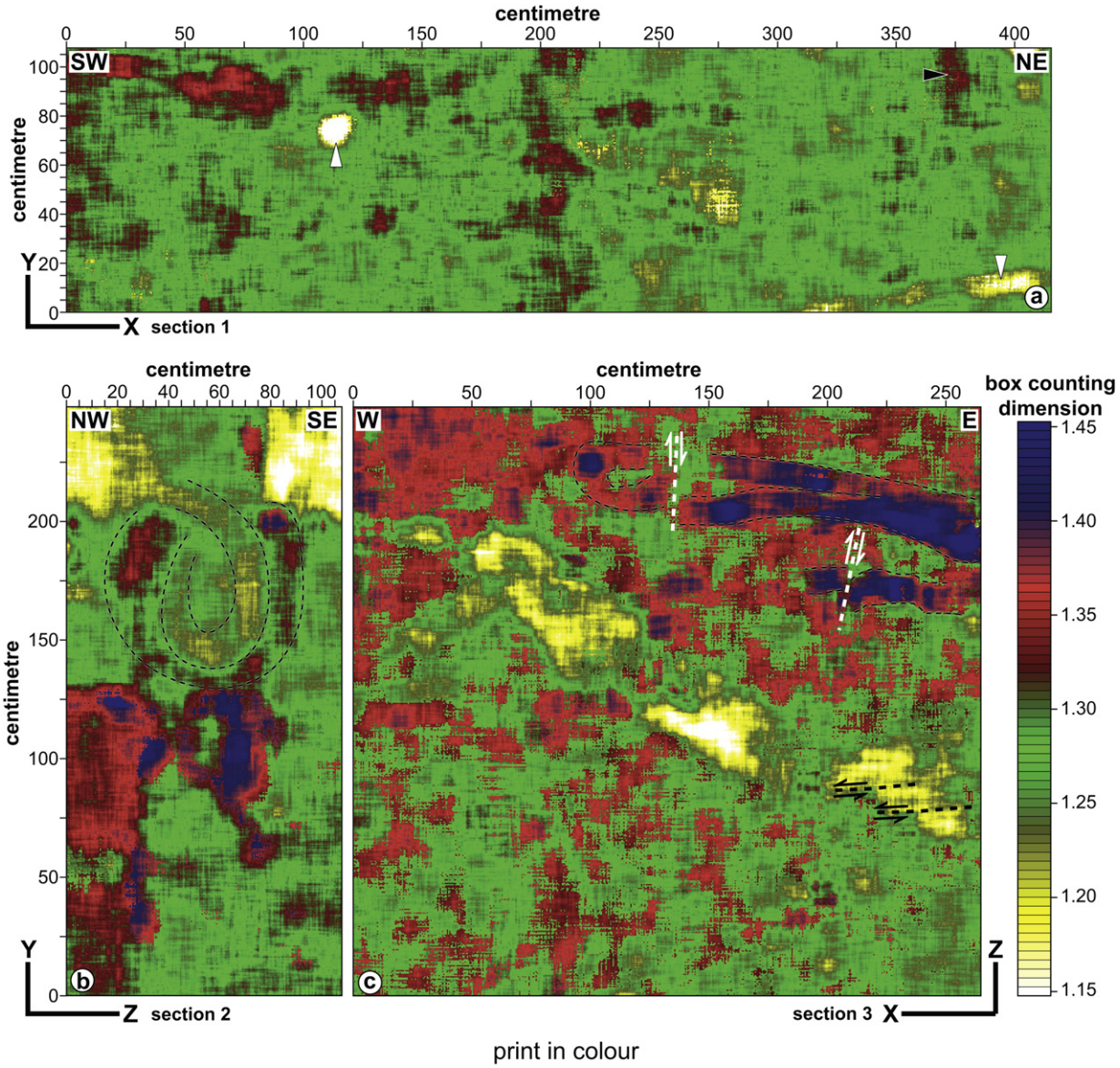

Fig. 10. Results of the high-resolution map-counting method applied to the mafic mineral-aggregate patterns from three orthogonal sections 1–3 of the Piquiri Syenite. Size r of the measurement window for map-counting = 10 cm, gliding distance s = 5 mm. The variation of box-counting dimension, represented by the colour map, reflects the inhomogeneity of the pattern's complexity. Low box-counting numbers indicate areas where mafic aggregates are geometrical well ("regular") organised to each other. Disorganised distribution of mafic aggregates, i.e. schlieren forming, leads to higher box-counting dimensions. Arrow heads in (a) mark areas where the results are influenced by a mafic enclave, crack and not photographed part. For interpretation of dashed and broken lines see text. The indexed colour intervals are 0.004. 190 900 measurements for (a), 110 400 for (b) and 254 400 for (c).

locally displaced (white dashed lines and arrows) and indicate dextral senses of movement. In addition, the upper planar structure is folded. Both, displacement and folding are not supported by our field observations, because the schlieren are locally very diffuse. On section 1 (Fig. 10a) irregular areas of high D_b values (red) are arranged in diffuse vertical and horizontal bands (Fig. 10a). The horizontal ones can be identified on the rock surface as schlieren-like structures, however, the vertical ones do not match field observations (Fig. 4a). The areas on section 1 with lowest pattern complexity – D_b values down to 1.0 – (Fig. 10a, white arrows) mark the positions of mafic microgranular enclaves and rock cracks deleted during image processing (Fig. 4a). One region of highest D_b is related to an artificial impurity (Fig. 10a, black arrow). Locally, the red to blue colours are arranged in ring-like or more irregular structures that can be correlated to folded and disrupted schlieren in the outcrop (compare Figs. 4b and 10b). Nevertheless, the upper ring structure of section 2 (Fig. 10b) is parallel to a region of low D_b values (yellow).

5.2. Anisotropy and its inhomogeneity

The results from the MORFA method applied on K-feldspar and mafic mineral-aggregate patterns are shown in Figs. 11 and 12. K-feldspar anisotropy intensities on sections 1 and 2 are within the same interval 1.00–1.40 (Fig. 11a, b, yellow–green colours, only in online version) and generally higher (up to 1.65) on section 3 (Fig. 11c). On sections 1 and 2, sub-vertical domains with relatively higher anisotropy intensities (up to 1.40 – green, only online version) are apparent (Fig. 11a, b). Comparatively low anisotropy intensity values (~1.00–1.20) occur on section 3 within the elongate more felsic part and approximately outline this body (compare Fig. 4c). The magmatic lineation, unveiled by the MCDM (black bars,

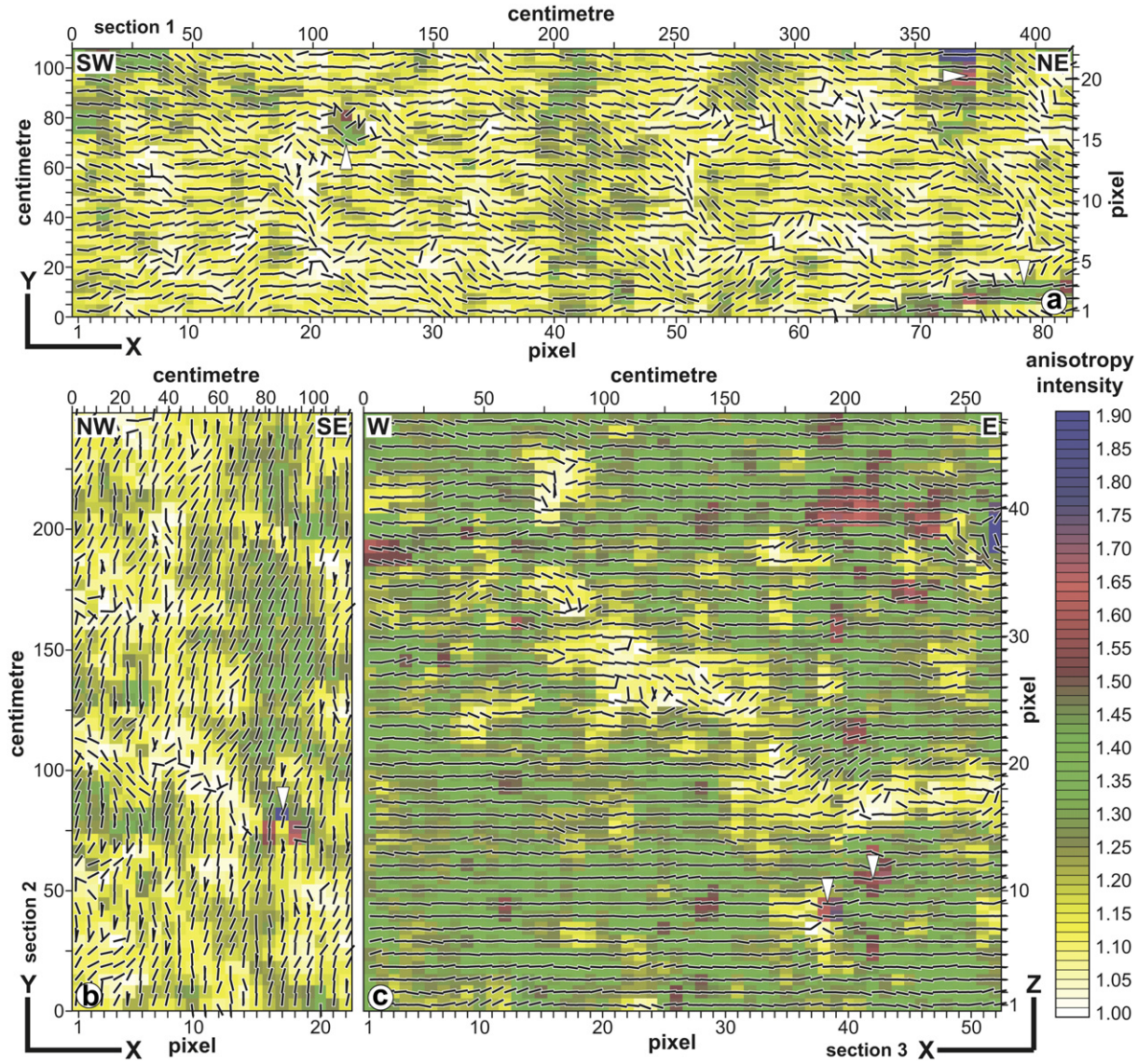

Fig. 11. High-resolution MORFA method applied to K-feldspar distribution patterns on the three syenite surfaces (section 1, 2 and 3, Figs. 3 and 4). The diameter *d* of the shifted circle is 20 cm, the gliding distance *s* is 5 cm. The anisotropy intensities are represented by colour-indexed pixels (Fig. 6b). The black bars represent the SAA. The value of *a*/*b* varies between 1 and roughly 1.70, with 1 indicating isotropy of the pattern and increasing values indicating increasing anisotropy The indexed colour intervals are 0.01. 1804 measurements for (a), 1034 for (b) and, 2444 for (c); Coloured figure available in the online version.

Fig. 11a), is almost horizontal, NE–SW oriented, but may deviate locally up to 70°. These deviations occur in up to 20 cm wide bands (Fig. 11a) that form a broad pattern in the m-scale. On sections 2 and 3 the black bars represent the SAA, based on the intersections of the planar feldspar crystals with the rock surface. On section 2 these directions are preferentially parallel to strain Y, and on section 3 preferentially parallel to strain-X (Fig. 11b, c). Of course, this is related to the fact that the flat faces of the K-feldspar crystals are well aligned perpendicular to strain-Z. Nevertheless, on both sections local deviations occur, which, on section 3, are mainly related to the felsic body (compare Fig. 4c).

The anisotropy intensities of the mafic aggregate patterns (Fig. 12) are slightly higher and more irregular in comparison to the feldspar ones, but in general smaller within sections 1 and 2 (~1.10–1.45, Fig. 12a, b) compared to section 3 (~1.45–1.90, Fig. 12c). No vertical substructure occurs within sections 1 and 2 as in case of the feldspars nor is the more felsic dyke-shaped domain (Fig. 4c) visible with section 3 (Fig. 12c). Similar to the results from the feldspar mineral patterns, the mafic aggregate SAAs are locally aligned within planar-shaped structures but they occur on different positions and appear to be more folded (Fig. 12, black lines).

6. Discussion

Since magmatic rock fabrics are (i) generally diffuse, (ii) mostly occur on scales above thin section or hand specimen, and (iii) are often inhomogeneous and anisotropic, quantification methods are required, which work with high precision on larger scales (several square metres and more) and are able to quantify fabric anisotropy as well as inhomogeneity. With map-counting the present study presents a fractal geometry method that has already proven suitable for these tasks on smaller scales (Peternell et al., 2003, 2010; Kruhl et al., 2004) and the new MORFA method based on MCDM (Kruhl et al., 2004; Volland and Kruhl, 2004) but with a non-fractal procedure (Gerik and Kruhl, 2009). It shows how these methods can be applied to larger regions of magmatic rock surfaces and, for

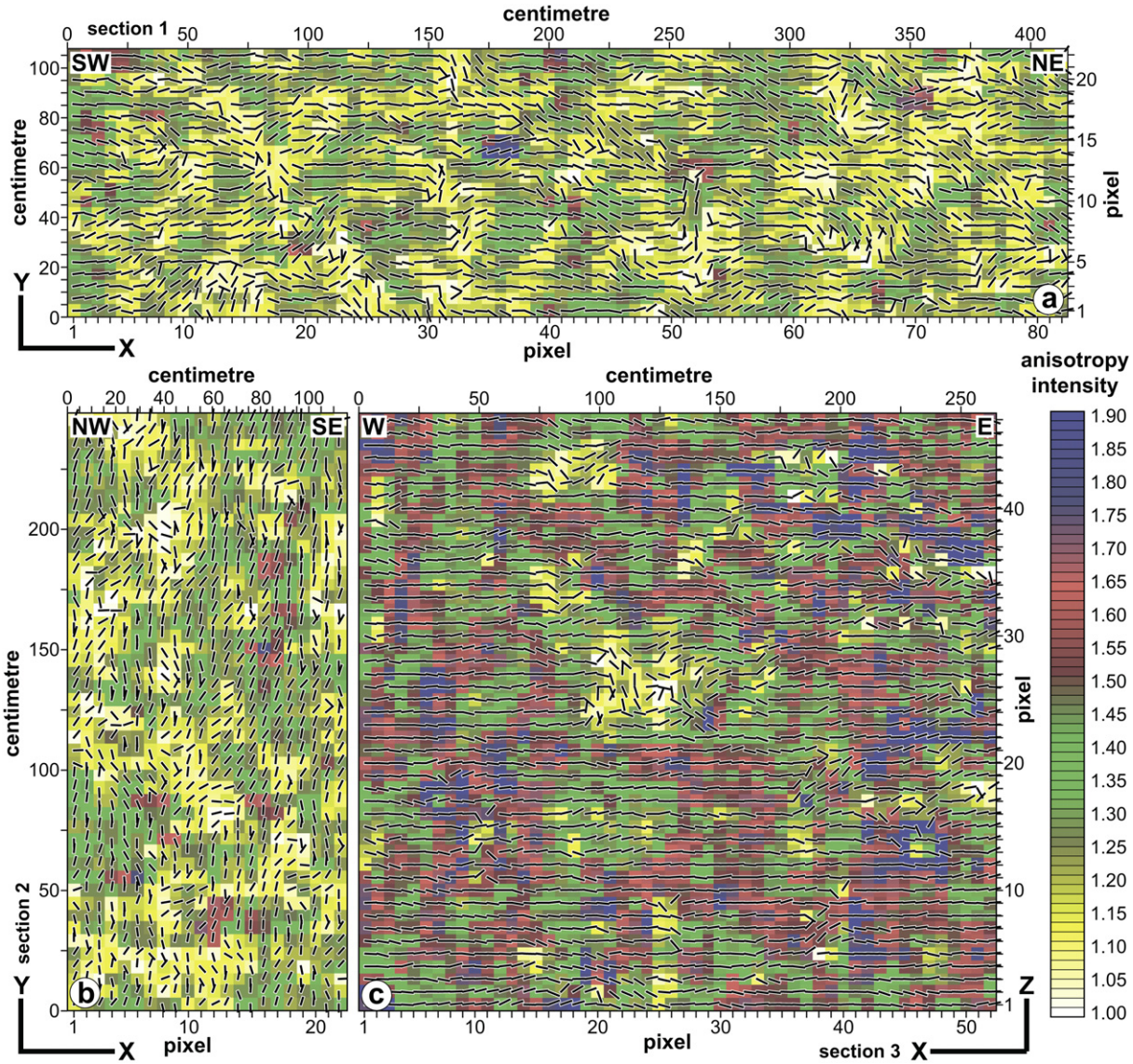

Fig. 12. High-resolution MORFA method applied to mafic mineral-aggregate distribution patterns on the three syenite surfaces (sections 1- 3, Fig. 4). The diameter *d* of the shifted circle is 20 cm, the gliding distance *s* is 5 cm. The anisotropy intensities are represented by colour-indexed pixels (Fig. 6b). The black bars represent the SAA. The value of *a*/*b* varies between 1 and roughly 1.70, with 1 indicating isotropy of the pattern and increasing values indicating increasing anisotropy. The indexed colour intervals are 0.01. 1804 measurements for (a), 1034 for (b) and, 2444 for (c); Coloured figure available in the online version.

the first time, a combined quantification and analysis of fabric inhomogeneity and anisotropy is performed.

Box-counting, applied to mafic mineral-aggregate patterns from the three rock surfaces parallel to the principal strain sections XZ, YZ and XY, proves the fractality, i.e. the self-similarity, of the pattern in the cm–mm-scale over ~1.5 orders of magnitude. The similar D_b values of 1.34 (D_b XZ), 1.36 (D_b YZ), and 1.37 (D_b XY) from the whole orthogonal sections suggest that the aggregate pattern is also fractal in 3D. However, with box-counting it is not possible to give information about spatial variations of fractality.

The range of D_b values of 0.3 (Fig. 10) revealed by map-counting, with $R^2 \geq 0.997$ for almost all the measurements, is much too large to be just 'background noise' (Supplementary material). Moreover, coarse structures of the D_b variation correlate with magmatic structures observed directly on the rock surfaces, such as the elongate felsic body in section 3 (Fig. 10c). Only areas of different D_b values, which are outlined in Fig. 10, correlate with areas of higher density of mafic mineral grains even if D_b is a measure of the area-filling ability of the pattern (Mandelbrot, 1982), this ability is more related to the geometric arrangement of the pattern than to its 'density', i.e. to the arrangement of mafic mineral grains or grain aggregates. It has been repeatedly shown in nature and experiment that crystal orientations and arrangements in magmatic rocks are generally the result of flow and crystallisation processes (Blumenfeld and Bouchez, 1988; Ildefonse and Fernandez, 1988; Vernon, 2000). In particular, the ring-like structure in section 2, the folded and displaced planar structures and the displaced areas correlating to schlieren and the elongate felsic body in section 3 (Fig. 10b, c) emphasise the importance of flow and shearing processes during crystallisation of the magma. Consequently, D_b – that quantifies the crystal patterns in the Piquiri Syenite Massif – provides information about the pattern-forming processes in the pluton, in agreement with observations from mathematical and natural patterns for example the Sierpinski triangle or fracture patterns (Feder, 1988; Bonnet et al., 2001). There are only a few other examples that use methods of fractal geometry to study the

relationship between crystal patterns (Armienti and Tarquini, 2002; Peternell and Kruhl, 2009) or mafic microgranular enclaves (Perugini and Poli, 2000) and magmatic processes.

The crystal arrangements which have been quantified by map-counting, were also investigated with respect to anisotropy. The SAA represented by the pattern of black bars in Figs. 10 and 11 is in general not necessarily related to crystal orientation or strain but to complexity of the pattern in a certain area. Nevertheless, in case of the investigated syenite pluton the SAAs are parallel to the SPOs of feldspar and mafic mineral aggregates. The application of MORFA to the distribution patterns of K-feldspar (Fig. 11) as well as mafic minerals (Fig. 12) leads to generally similar but locally different results. Three different types of regions can be distinguished:

(1) Relatively broad areas of several decimetres, up to 1 m in diameter and with constant orientation of SAAs. This SPO defines the subhorizontal magmatic lineation on the strain XY parallel planes (Figs. 11a and 12a, Section 4.3). On sections 2 and 3 it coincides with the intersection lines of K-feldspars and mafic mineral aggregates (the latter partly determined by the K-feldspar shapes) with the rock surfaces. The alignment of SAAs is clearly stronger on section 3 compared to section 2. This probably reflects the fact that the sections of crystals or crystal aggregates are more compact on section 2 and more elongate on section 3.
(2) In smaller and more irregularly outlined areas the SAA varies largely. In some cases it is strongly but regularly deviating from the main orientation, in other cases the SAA is highly variable. On section 3 these areas correlate roughly but not completely with the felsic body (Figs. 4c, 11c and 12c) and locally a rough correlation with mafic schlieren structures is visible, for example with a moderately SE dipping darker band in the central lower part of section 2 (between 50 and 100 cm vertical; Figs. 4b, 11b and 12b). However, in general no correlations with field structures are visible. In certain cases the areas in the K-feldspar patterns coincide with those in the mafic mineral patterns, but in many cases they do not.
(3) The first two types of areas are often separated by more elongate areas (bands) with decimetre width and up to 1 m length and with one dominant SAA, different from the 'main' orientation (type one). These areas are most prominent on section 1 and much less on sections 2 and 3. They are roughly equally developed in the K-feldspar and mafic mineral patterns and there are no corresponding structures visible in the field. Interestingly these bands exhibit some regularity. They are mostly oriented at $\sim 45^{\circ}$ to the main SAA outside the bands, specifically on section 1, and in general but not always SAAs are parallel to the bands. Sometimes the changes in SAA from outside to inside the bands are sharp and in the bands the orientations are strictly parallel. These structures are not visible on the rock surfaces. Since they closely resemble conjugate shear bands in deformed rocks, the question arises if they could represent similar features in magmatic rocks: zones of increased shear in the crystal-melt mush, zones of increased rate of flow, or even former fracture systems that enabled fluid/melt migration through the magmatic body (Walker, 1969; Berger and Pitcher, 1970; Barbarin and Didier, 1992; Büttner, 1999) and thus changed the rheology and reactivity of the crystal-melt mush (Hess and Dingwell, 1996; Giordano et al., 2004). Following this line of argument, the areas with more irregular bar orientation are interpreted as variations in the flow field direction.

Could the variation in SAA, outlined above, not simply be caused by a low ellipticity of the point distribution (Fig. 8b) leading to a large error in orientation of the ellipse's principal axes a and b? This cannot completely be ruled out for those areas with anisotropy intensities below ~ 1.10 (Figs. 11 and 12). However, many of the areas with disturbed SAAs show such pattern anisotropies with values over 1.30 (green). In addition, no evidence that might cause artificial orientation patterns is visible on the image processed grey-scale templates used for the analysis (Fig. 6). Also, the high correlation coefficient of >0.9 for the elliptical fit argues against a significant error in orientation of the ellipses' axes. The bands of aligned SAAs show anisotropy intensities partly in the same range, and locally even above, as the areas of main alignment. Again, this points to the relevance of these features.

7. Conclusions

Based on high resolution and large-scale recording and quantification of mineral distribution patterns in a syenite pluton, the present study shows:

(1) Modified and partly automated methods, such as map-counting and the mapping of rock fabric anisotropy (MORFA) method, are suitable for quantifying and analysing complex and diffuse meso-scale magmatic fabrics over large areas (several square metres and more).
(2) Map-counting procedures on a decimetre to metre scale unveils diffuse structures that can be related to mafic schlieren or felsic dykes that are not visible on the rock surfaces. MORFA leads to the detection of the mineral shape preferred orientation, i.e. a magmatic lineation and its variation over large areas, which are not visible in the field.
(3) With MORFA mineral distribution fabrics on a decimetre to metre scale, with different intensity and orientation of alignment are determined. Such fabrics, not visible in the field, can only be determined using such high-resolution analysis.
(4) These fabrics possibly represent flow or fracture structures that developed in the crystallising magma. Therefore, applications of automated fabric-analysing methods, such as map-counting and MORFA, open a new field of structural investigation to magmatic rocks.

Acknowledgements

Many thanks are due to Tom Blenkinsop and an anonymous reviewer for their reviews which highly improved the paper. Financial support by the Leonhard-Lorenz Foundation (grant 629/04) for MP, by FAPERGS (Rio Grande do Sul State Research Foundation) and CNPq (Brazilian Research Council) for MFB and by the German Academic Exchange Service (DAAD) for JHK are gratefully acknowledged. Many thanks are due to Chris Wilson for many constructive comments on the manuscript and to Axel Gerik and Christian Schneider who programmed algorithms for automating the map-counting and MORFA method. Thanks are also due to Kurt Doppler for construction of a special tripod for field photographs, to Vladimir Ruttner for preparation of the thin sections, and to Monika Nießing for stitching together the field photographs.

Appendix. Supplementary data

Supplementary data associated with this article can be found, in the online version, at doi:10.1016/j.jsg.2011.01.011.

References

Albertz, M., 2006. Relationships between melt-induced rheological transitions and finite strain: observations from host rock pendants of the Tuolumne Intrusive Suite, Sierra Nevada, California. Journal of Structural Geology 28, 1422–1444.

Armienti, P., Tarquini, S., 2002. Power law olivine crystal size distributions in lithospheric mantle xenoliths. Lithos 65, 273–285.

Büttner, S.H., 1999. The geometric evolution of structures in granite during continuous deformation from magmatic to solid-state conditions: an example from the central European Variscan Belt. American Mineralogist 84, 1781–1792.

Barbarin, B., Didier, J., 1992. Genesis and evolution of mafic microgranular enclaves through various types of interaction between coexisting felsic and mafic magmas. Transactions Royal Society Edinburgh, Earth Sciences 83, 145–153.

Berger, A.R., Pitcher, W.S., 1970. Structures in granitic rocks, a commentary and critique of granite tectonics. Proceedings of the Geologists' Association 81, 441–461.

Blumenfeld, P., Bouchez, J.L., 1988. Shear criteria and migmatite deformed in the magmatic and solid states. Journal of Structural Geology 10, 361–372.

Bonnet, E., Bour, O., Odling, N.E., Davy, P., Main, I., Cowie, P., Berkowitz, B., 2001. Scaling of fracture systems in geological media. Reviews of Geophysics 39, 347–383.

Brown, M., 2007. Crustal melting and melt extraction, ascent and emplacement in orogens: mechanisms and consequences. Journal of the Geological Society of London 164, 709–730.

D'Lemos, R.S., Brown, M., Strachan, R.A., 1992. Granite magma generation, ascent and emplacement within a transpressional orogen. Journal of the Geological Society of London 149, 487–490.

Feder, J., 1988. Fractals. Plenum Press, New York.

Ford, A., Blenkinsop, T.G., 2008. Evaluating geological complexity and complexity gradients as controls on copper mineralisation, Mt Isa Inlier. Australian Journal of Earth Sciences 55, 13–23.

Gaillot, P., Darrozes, J., de Saint Blanquat, M., Ouillon, G., 1997. The normalized optimized anisotropic wavelet coefficient (NOAWC) method: an image processing tool for multiscale analysis of rock fabric. Geophysical Research Letters 24, 1819–1822.

Gerik, A., Kruhl, J.H., 2009. Towards automated pattern quantification: time-efficient assessment of anisotropy of 2D patterns with AMOCADO. Computers & Geosciences 35, 1087–1097.

Giordano, D., Romano, C., Poe, B., Dingwell, D.B., Behrens, H., 2004. The combined effects of water and fluorine on the viscosity of silicic magmas. Geochimica Cosmochimica Acta 68, 5159–5168.

Hess, K.H., Dingwell, D.B., 1996. Viscosities of hydrous leucogranitic melt: a non-Arrhenian model. American Mineralogist 81, 1297–1300.

Higgins, M.D., 1996. Magma dynamics beneath Kameni Volcano, Thera, Greece, as revealed by crystal size and shape measurements. Journal of Volcanology and Geothermal Research 70, 37–48.

Higgins, M.D., 2000. Measurement of crystal size distributions. American Mineralogist 85, 1105–1116.

Hirata, T., 1989. Fractal dimension of fault systems in Japan: fractal structure in rock fracture geometry at various scales. Pure and Applied Geophysics 131, 157–170.

Hodkiewicz, P.F., Weinberg, R.F., Gardoll, S.J., Groves, D.I., 2005. Complexity gradients in the Yilgarn Craton: fundamental controls on crustal-scale fluid flow and the formation of world-class orogenic-gold deposits. Australian Journal of Earth Sciences 52, 831–841.

Hollister, L.S., Crawford, M.L., 1986. Melt-enhanced deformation: a major tectonic process. Geology 14, 558–561.

Hutton, D.H.W., 1982. A tectonic model for the emplacement of the main donegal granite, NW Ireland. Journal of the Geological Society of London 139, 615–631.

Ildefonse, B., Fernandez, A., 1988. Influence of the concentration of rigid markers in a viscous medium on the production of preferred orientations: an experimental contribution. Bulletin of the Geological Institutions of the University of Uppsala, New Series 14, 55–60.

Kaye, B.H., 1989. A Random Walk through Fractal Dimensions. VCH, New York.

Kim, I.K., Jung, D.W., Park, R.H., 2002. Document image binarization based on topographic analysis using a water flow model. Pattern Recognition 35, 265–277.

Kruhl, J.H., Nega, M., 1996. The fractal shape of sutured quartz grain boundaries: application as a geothermometer. Geologische Rundschau 85, 38–43.

Kruhl, J.H., Andries, F., Peternell, M., Volland, S., 2004. Fractal geometry analyses of rock fabric anisotropies and inhomogeneities. In: Kolymbas, D. (Ed.), Fractals in Geotechnical Engineering. Advances in Geotechnical Engineering and Tunnelling 9. Logos, Berlin, pp. 115–135.

Launeau, P., Cruden, A.R., 1998. Magmatic fabric acquisition mechanisms in a syenite: results of a combined anisotropy of magnetic susceptibility and image analysis study. Journal of Geophysical Research 103, 5067–5089.

Launeau, P., Robin, P.Y.F., 1996. Fabric analysis using the intercept method. Tectonophysics 267, 91–119.

Mandelbrot, B.B., 1967. How long is the coast of Britain? Statistical self-similarity and fractional dimension. Science 156, 636–638.

Mandelbrot, B.B., 1977. Fractals. W.H. Freeman and Company, San Francisco.

Mandelbrot, B.B., 1982. The Fractal Geometry of Nature. Freeman & Co., New York, 468 pp.

Marsh, B.D., 1988. Crystal size distribution (CSD) in rocks and the kinetics and dynamics of crystallization. 1, Theory. Contributions to Mineralogy and Petrology 99, 277–291.

Martín-Hernández, F., Luneburg, C., Aubourg, C., Jackson, M. (Eds.), 2005. Magnetic Fabric: Methods and Applications. Geological Society Special Publications 238.

Nardi, L.V.S., Plá Cid, J., Bitencourt, M.F., 2007. Minette mafic microgranular enclaves and their relationship to host syenites in systems formed at mantle pressures: major and trace element evidence from the Piquiri Syenite Massif, southernmost Brazil. Mineralogy and Petrology 91, 101–116.

Nardi, L.V.S., Plá Cid, J., Bitencourt, M.F., Stabel, L.Z., 2008. Geochemistry and petrogenesis of post-collisional ultrapotassic syenites and granites from southernmost Brazil: the Piquiri Syenite Massif. Anais da Academia Brasileira de Ciências 80, 353–371.

Panozzo, R., 1987. Two-dimensional strain determination by the inverse SURFOR wheel. Journal of Structural Geology 9, 115–119.

Paterson, S.R., Vernon, R.H., Tobisch, O.T., 1989. A review of criteria for the identification of magmatic and tectonic foliations in granitoids. Journal of Structural Geology 11, 349–363.

Paterson, S.R., Fowler, T.K., Schmidt, K.L., Yoshinobu, A.S., Yuan, E.S., Miller, R.B., 1998. Interpreting magmatic fabric patterns in plutons. Lithos 44, 53–82.

Perugini, D., Poli, G., 2000. Chaotic dynamics and fractals in magmatic interaction processes; a different approach to the interpretation of mafic microgranular enclaves. Earth and Planetary Science Letters 175, 93–103.

Peternell, M., 2007. Fabric patterns in magmatic rocks: method development, automation and geological significance. Ph.D. thesis, Technische Universität München.

Peternell, M., Kruhl, J.H., 2009. Automation of pattern recognition and fractal-geometry-based pattern quantification, exemplified by mineral-phase distribution patterns in igneous rocks. Computers & Geosciences 35, 1415–1426.

Peternell, M., Andries, F., Kruhl, J.H., 2003. Magmatic flow-pattern anisotropies – analyzed on the basis of a new 'map-counting' fractal geometry methodInternational Conference; Geology without Frontiers; Magmatic and Metamorphic Evolution of Central European Variscides; Abstract vol. 48. Journal of the Czech Geological Society, Czech Republic, 104.

Peternell, M., Bitencourt, M.F., Kruhl, J.H., Stäb, C., 2010. Macro and microstructures as indicators of the development of syntectonic granitoids and host rocks in the Camboriú region, Santa Catarina, Brazil. Journal of South American Earth Sciences 29, 738–750.

Petford, N., Cruden, A.R., McCaffrey, K.J.W., Vigneresse, J.L., 2000. Granite magma formation, transport and emplacement in the Earth's crust. Nature 408, 669–673.

Philipp, R.P., Machado, R., Nardi, L.V.S., Lafon, J.M., 2002. O magmatismo granítico neoproterozóico do Batólito Pelotas no sul do Brasil: novos dados e revisão da geochronologia regional. Revista Brasileira de Geociências 32, 277–290.

Piazolo, S., Passchier, C.W., 2002. Controls on lineation development in low to medium grade shear zones: a study from the Cap de Creus peninsula, NE Spain. Journal of Structural Geology 24, 25–44.

Porcher, C.A., 2000. Programa Levantamentos Geológicos Básicos do Brasil, Folha Cachoeira SH.22-Y-A. Estado do Rio Grande do Sul. Brasília, CPRM, 131p. Escala 1, 250000.

Rochette, P., Jackson, M., Aubourg, C., 1992. Rock magnetism and the interpretation of anisotropy of magnetic susceptibility. Reviews of Geophysics 30, 209–226.

Rosenberg, C., 2001. Deformation of partially molten granite: a review and comparison of experimental and natural case studies. International Journal of Earth Sciences 90, 60–76.

Rosenberg, C.L., Handy, M.R., 2005. Experimental deformation of partially melted granite revisited: implications for the continental crust. Journal of Metamorphic Geology 23, 19–28.

Smit, T.H., Schneider, E., Odgaard, A., 1998. Star length distribution: a volume-based concept for the characterization of structural anisotropy. Journal of Microscopy 191, 249–257.

Takahashi, M., Nagahama, H., Masuda, T., Fujimura, A., 1998. Fractal analysis of experimentally, dynamically recrystallized quartz grains and its possible application as a strain rate meter. Journal of Structural Geology 20 (2–3), 269–275.

Tarling, D.H., Hrouda, F., 1993. The Magnetic Anisotropy of Rocks. Chapman & Hall, London.

Tröger, W.E., 1952. Optische Bestimmung der gesteinsbildenden Minerale, Teil 1: Bestimmungstabellen. Schweizerbart'sche Verlagsbuchhandlung, Stuttgart.

Turcotte, D.L., 1989. Fractals in geology and geophysics. Pure and Applied Geophysics 131, 171–196.

Velde, B., 1999. Structure of surface cracks in soil and muds. Geoderma 93, 101–124.

Velde, B., Dubois, J., Touchard, G., Badri, A., 1990. Fractal analysis of fractures in rocks: the Cantor's dust method. Tectonophysics 179, 345–352.

Vernon, R.H., 2000. Review of microstructural evidence of magmatic and solid-state flow. Electronic Geosciences 5:2.

Vincent, L., Soille, P., 1991. Watersheds in digital spaces: an efficient algorithm based on immersion simulations. IEEE Transactions on Pattern Analysis and Machine Intelligence 13, 583–598.

Volland, S., Kruhl, J.H., 2004. Anisotropy quantification: the application of fractal geometry methods on tectonic fracture patterns of a Hercynian fault zone in NW Sardinia. Journal of Structural Geology 26, 1499–1510.

Walker, G.P.L., 1969. The breaking of magma. Geological Magazine 106, 166–173.

Walsh, J.J., Watterson, J., 1993. Fractal analysis of fracture patterns using the standard box-counting technique: valid and invalid methodologies. Journal of Structural Geology 15, 1509–1512.

Zak, J., Paterson, S.R., Memeti, V., 2007. Four magmatic fabrics in the Tuolumne Batholith, central Sierra Nevada, California (USA): implications for interpreting fabric patterns in plutons and evolution of magma chambers in the upper crust. Geological Society of America Bulletin 119, 184–201.